Nanoscale

PAPER

Published on 24 March 2026
Licensed under CC-BY 4.0

Check for updates

Cite this: *Nanoscale*, 2026, **18**, 10307

Upconverting mixed emitter nanocomposites as sensitive luminescent thermometers within plant-inspired artificial fliers

Albenc Nexha, [a] Stefano Mariani, [b] Anja Colbus,[a] Kliton Cikalleshi, [b,c] Barbara Mazzolai *[b] and Tobias Kraus *[a,d]

Received 4th February 2026,
Accepted 23rd March 2026

DOI: 10.1039/d6nr00489j

rsc.li/nanoscale

The applicability of current upconverting lanthanide-doped luminescent thermometers is limited by signal discriminability and thermal sensitivity. We overcome these limitations by creating fluorescent nanocomposites in biodegradable polyhydroxyalkanoates (PHAs). Nanocomposites that combine different lanthanide-based upconverting nanoparticles were designed. We created mixed emitter composites with bright red (Mn^{2+} doped with Er^{3+} and Yb^{3+} in $NaYF_4$), green (Er^{3+} and Yb^{3+} in $BaYF_5$) and blue (Tm^{3+} and Yb^{3+} in CaF_2) emitting particles to obtain clearly distinguishable and intense fluorescence signals. The resulting nanocomposites had maximum relative thermal sensitivities of 34% K^{-1}, outperforming existing thermometers. Importantly, their readout requires detection only in visible wavelength ranges, making them particularly suitable for drone-based environmental monitoring purposes. To demonstrate their applicability in this field, we integrated the nanocomposites into plant-inspired artificial fliers, creating self-deployable and biocompatible units for wireless monitoring of environmental temperature. The surface temperature of topsoil was reconstructed based on the fluorescence intensity ratio among the RGB (red-green-blue) wavelengths of the upconverting nanocomposites integrated into the fliers.

Introduction

Upconverting lanthanide-doped materials (Ln^{3+}) can convert low-energy near infrared (NIR) excitation into high energy emitting lights, spanning from ultraviolet (UV), visible (Vis) and NIR regions.[1] Their luminescence properties, such as intensity, spectral position, bandwidth, band shape, lifetime and polarization, are temperature-dependent, allowing for the application of these materials as luminescent thermometers.[2,3] These thermometers are able to detect temperature changes in a non-intrusive mode, combined with high accuracy, nanoscale spatial resolution and fast temporal response.[2,3] Due to these abilities, Ln^{3+} ions are continuously being investigated and developed for multiple applications ranging from biomedicine to photovoltaics.[1–3] Ongoing trials are devoted to the preparation of highly reliable and sensitive upconverting emitters.

The readout of such thermometers with band-shape or ratiometric techniques exploits the change of intensity ratios between two emission bands with temperature.[2] Ratiometric data are less affected by the optical setup, the concentration of the emitting ions and background signals from other emitters or light sources.[2] Most of the existing ratiometric thermometers are based on the thermally coupled levels (TCLs) of single emitting Ln^{3+} ions.[2–4] TCLs are closely spaced energy levels within an ion that are in thermal equilibrium.[2–4] Their performance can be quantified using the relative thermal sensitivity (S_{rel}, in % K^{-1} units), a figure of merit that is independent of the characteristics of the materials (structure and morphology), operating wavelengths, or acquisition setups.[2,3] The S_{rel} of TCL-based thermometers is limited by the energy gap (ΔE) of the coupled levels, which is relatively small and in the range of 200–2000 cm^{-1}.[1,2–4] For example, the thermometric performance of upconverting Er^{3+}-doped materials based on the green TCL emissions of $^2H_{11/2}$ and $^4S_{3/2}$ TCLs is generally below 1.5% K^{-1}.[4] Tm^{3+}- or Nd^{3+}-doped thermometers based on TCLs (Tm^{3+}: $^3F_{2,3}$ and $^3H_4$ and Nd^{3+}: Stark sublevels of the $^4F_{3/2}$ multiplet) exhibit sensitivities below 1% K^{-1}.[2–4] Furthermore, the small ΔE of the emission can cause spectral overlap,[5–7] which makes detection harder and limits the signal-to-noise ratio (SNR).

Dual emitting ions with opposite temperature-dependent luminescence properties have been used to overcome these limitations in ratiometric sensing. For example, co-doping a host with Eu^{3+} and Tb^{3+} emitters can improve the SNR and the thermometric performance,[8–10] but only at cryogenic temperatures upon excitation with (phototoxic) UV light. Other thermometers based on Ho^{3+} and Tm^{3+} co-emitters are ther-

[a]*INM-Leibniz Institute for New Materials, 66123 Saarbrücken, Germany. E-mail: tobias.kraus@leibniz-inm.de*
[b]*Bioinspired Soft Robotics Laboratory, Istituto Italiano di Tecnologia, Italy*
[c]*The Biorobotics Institute, Scuola Superiore Sant'Anna, 56025 Pontedera, Italy*
[d]*Saarland University, Colloid and Interface Chemistry, 66123 Saarbrücken, Germany*

mally stable and can be excited with NIR, but their maximum S_{rel} is around 2% K^{-1}.[11,12] Hybrid structures composed of quantum dots and Ln^{3+} have moderate S_{rel} values in the range of 3% K^{-1},[13,14] but their performance is drastically hampered by the limited environmental stability of the quantum dots.[3] Therefore, the quest for thermometers with high sensitivities and easy readout is still ongoing.

Recently, strategies for integrating dual emitting Ln^{3+} ions that combine positive (a decrease in the intensity of emission with temperature, *i.e.* quench "off") and negative (an increase in the intensity of emission with temperature, *i.e.* quench "on") thermal quenching have been shown to boost thermometric performance.[15] Such thermometers combine two different hosts, for example, Er^{3+} with green emission at 540 nm in Er^{3+} and Yb^{3+}:$NaYF_4$@$NaYF_4$ core@shell nanoparticles combined with Tm^{3+}:$Yb_2W_3O_{12}$ particles where Tm^{3+} emits at 796 nm. The two emitters were integrated into hydrogels, and the combination of quench "off" (Er^{3+}, 540 nm) and quench "on" (Tm^{3+}, 796 nm) resulted in a maximum sensitivity up to 23.84% K^{-1} at 380 K.[15] Similar results were obtained when the 540 nm emission of Er^{3+} was combined with the emission of Nd^{3+} ions (at 799 nm within a Nd^{3+}:$Yb_2W_3O_{12}$ matrix), with a sensitivity above 5% K^{-1} in the range from 350 K to 450 K, reaching a maximum of 15.3% K^{-1} at 380 K.[15] The $Yb_2W_3O_{12}$ host has to be prepared by calcinating the precursors at 1273 K, resulting in microparticles with diameters of around 3 μm and heterogeneous doping. The quench "on" mechanisms are sensitive to the concentration of the emitting ions, requiring extensive optimization for thermometry.[15] Finally, the readout of these thermometers required concurrent measurements in the Vis and NIR regions. We are interested in upconverting emitters that enable thermometry with high sensitivities, can be combined in a modular fashion, and only require recording RGB (red-green-blue) wavelengths so that the readout is possible with standard colour cameras.

Herein, we combine nanoparticles with positively thermally quenched levels of Ln^{3+} and embed them into a polyhydroxyalkanoate (PHA) polymer matrix, a biodegradable and non-toxic polymer.[16,17] Bright red (Mn^{2+}-doped Er^{3+} and Yb^{3+} in $NaYF_4$), green (Er^{3+} and Yb^{3+} in $BaYF_5$) and blue (Tm^{3+} and Yb^{3+} in CaF_2) emitting nanoparticles are designed to prepare nanocomposites with high SNRs, clearly distinguishable fluorescent signals and high S_{rel}. We use them as luminescent thermometers in plant-inspired artificial fliers, a class of 3D printed structures that mimic the properties of natural plant seeds,[18,19] to monitor the temperature of topsoil. We 3D print artificial fliers inspired by natural *Acer campestre* seeds[18] and integrate fluorescent nanocomposites built on the mixed emitters to monitor the surface temperature of topsoil in the range of 268–313 K.

Experiments

Chemicals and materials

All precursors were purchased from Sigma-Aldrich (Germany). All chemicals were used without further purification. Polyhydroxyalkanoate (PHA) filaments were purchased from ColorFabb (Germany). Ethyl cyanoacrylate glue was purchased from Loctite, Henkel Corporation (Germany).

Synthesis of upconverting nanoparticles

The upconverting particles were prepared *via* published solvothermal routes.[20–22] For the red emitting particles,[21] an aqueous dispersion (2.6 mL in total) containing Mn$(NO_3)_2{\cdot}4H_2O$ (0.3 mmol), $Y(NO_3)_3{\cdot}6H_2O$ (0.5 mmol), Yb$(NO_3)_3{\cdot}5H_2O$ (0.18 mmol) and $Er(NO_3)_3{\cdot}5H_2O$ (0.02 mmol) was added to a mixture of oleic acid (16 mmol), NaOH (7.5 mmol) and distilled water (1.5 mL). After continuous stirring for 10 min, 4 mmol NaF in 2 mL of distilled water were added dropwise to the mixture, followed by additional stirring for 30 min. The dispersion was transferred into a Teflon-lined autoclave reactor and heated at 200 °C for 8 h.

For the green emitting particles,[20] 0.5 mmol of an aqueous dispersion (1 mL in total) of rare earth nitrates (2 mol% Er$(NO_3)_3{\cdot}5H_2O$, 20 mol% $Yb(NO_3)_3{\cdot}5H_2O$ and 78 mol% $Y(NO_3)_3{\cdot}5H_2O$) and 0.5 mmol of an aqueous dispersion (3 mL in total) of $Ba(NO_3)_2{\cdot}5H_2O$ were added to a vial containing oleic acid (64 mmol), ethanol (10 mL), NaOH (15 mmol) and distilled water (2 mL). After stirring for 10 minutes, NH_4F (4 mmol) dispersed in distilled water (1 mL) was added to the mixture. The mixture was transferred to a Teflon-lined autoclave reactor and heated at 210 °C for 24 h.

For the blue emitting particles,[22] aqueous solutions (1 mL in total) of 0.5 mmol of nitrate salts (0.5 mol% Tm$(NO_3)_3{\cdot}5H_2O$, 20 mol% $Yb(NO_3)_3{\cdot}5H_2O$ and 78 mol% $Y(NO_3)_3{\cdot}5H_2O$) and 2 mmol of NaF (in 4 mL of distilled water) were added to a mixture of oleic acid (20 mL), ethanol (8 mL), NaOH (1.2 g) and deionized water (8 mL). The mixture was transferred to a Teflon-lined autoclave reactor and heated at 180 °C for 36 h.

The purification process was identical for all the upconverting particles. After the autoclave reactor had cooled down to room temperature, the nanoparticles were collected after washing several times with ethanol, followed by centrifugation and redispersion in organic solvents.

Preparation of fluorescent composites

Fluorescent nanocomposites were prepared using a solvent evaporation process.[18,19] Approximately 1 g of polyhydroxyalkanoate (PHA) polymer was dissolved in chloroform (approximately 10 mL) aided by vortex and ultrasound. Single emitting particles (blue, green and red) and mixed particles (blue/green, blue/red, and green/red) at different concentrations were added to the PHA dispersion. After continuous stirring for approximately one hour, a uniformly dispersion was obtained. Then, around 2 mL of each composition was deposited into a Teflon template (circular shape, 10 cm in diameter). The solution was allowed to dry at room temperature to yield a fluorescent composite. Smaller disc-like composites with diameters of 8.0 ± 0.7 mm were prepared using a Peddinghaus punch set.

This journal is © The Royal Society of Chemistry 2026

Characterization of fluorescent materials and composites

Fluorescent nanocomposites were prepared using a solvent evaporation method, and transmission electron microscopy (TEM, JEOL JEM2100) operating at an acceleration voltage of 200 kV was used to determine the size and shape of the upconverting nanoparticles. TEM specimens were prepared by depositing around 20 μL of a diluted dispersion of the nanoparticles on the surface of a carbon-coated copped grid. The size of the nanoparticles was determined using ImageJ software after analyzing over 100 nanocrystals. Scanning electron microscopy (SEM) and energy dispersive X-ray spectroscopy (EDX) were performed using a Quanta 400ESEM (FEI Technologies Inc.) equipped with an EDX detector from Oxford Instruments. An acceleration voltage between 1 kV and 15 kV was used to acquire data. The crystalline structure of the fluorescent materials was characterized by X-ray powder diffraction (XRPD) using a D8 Advance diffractometer with a CuK_α radiation source (λ = 1.54060 Å, 40 kV, 40 mA) in a 2θ range from 10° to 80° at a scan rate of 0.02° per second. Raman spectroscopy was employed to characterize the vibrational modes of the fluorescent materials. A Renishaw inVia microscope with unpolarized light from a 532 nm argon laser was focused on the materials using a 50× objective. Analysis was performed within the range of 100–2000 cm^{-1} using a grating with 2400 lines per mm and an exposure time of 10 s. The photoluminescence of the fluorescent nanoparticles and nanocomposites was analysed by recording the emission spectra using an FS5 Edinburgh Instruments spectrofluorometer equipped with an external 980 nm NIR laser source placed perpendicular to the position of the fluorescent materials and composites. The emission spectra were obtained within the range from 400 nm to 800 nm with a resolution of 2 nm and an integration time of 0.5 s.

Production and characterization of the fluorescent flying seeds

Natural *Acer campestre* seed morphometric analysis. The morphometric and aerodynamic features of the seeds were determined following the methodology outlined in our earlier research.[18] In summary, seeds of *Acer campestre* were collected from a tree located in a rural area near Florence, Italy. Morphological measurements were performed using a digital caliper (RS PRO 150 mm Digital Caliper) and a digital microscope (KH-8700). The seed mass was determined using an analytical balance (KERN ABS-N) with a sensitivity of ±0.0001 g. These measurements were based on 10 distinct seeds. The morphological characteristics influencing the flight performance included the wing surface area (S) and the wing loading (W/S). For these parameters, data were collected from 8 individual seeds. The wing surface area (S) was derived from the images of 10 *Acer campestre* seeds captured using the 1280 × 800-pixel camera of a Samsung A40 smartphone. Image analysis was carried out with ImageJ software,[23] where images were binarized, and S was estimated by counting black pixels within a known 2 cm scale bar. W/S was calculated using the measured seed weight (W) and the corresponding S.

Determination of the indoor aerodynamic performance of the natural *Acer campestre* seeds. The aerodynamic analysis of natural seeds under controlled laboratory conditions focused on quantifying key flight-related parameters, namely descent speed (v_d), rotational velocity (Ω), wing tip speed (v_t), and conic angle (β).[24,25] To assess v_d, *Acer campestre* seeds were released from a height of 2.95 meters in still air, ensuring no ventilation was present in the room. Their descent was captured using a Xiaomi Redmi Note 5 smartphone, featuring a 1920 × 1080-pixel resolution. The v_d was calculated by measuring the time interval from the moment of release to the moment the seed comes into contact with the ground, as determined from the video frames. Each of the 10 seeds was dropped three times, resulting in a total of 30 trials. The same setup was adapted to determine Ω and v_t. For this purpose, videos were recorded using an Apple iPhone 12 Pro Max at a frame rate of 240 fps (equivalent to 4.17 milliseconds between frames) with a resolution of 1280 × 800 pixels. This procedure was also used to estimate β, which results from the interplay among the centrifugal force acting on the distributed mass, the gravitational force, and aerodynamic forces that induce torque about the flapping x axis.[24,25]

Design and fabrication of the artificial *Acer campestre* seeds. The design of the artificial *Acer campestre* seeds was based on a previously reported method.[18] Briefly, a top-view image of a natural *Acer campestre* samara was used in conjunction with the dimensional data previously reported.[18] The outline of the seed was traced and vectorized using Affinity Designer (trial version), and the resulting file was imported into Siemens NX, a 3D CAD modeling software, and scaled to develop the 2× artificial *Acer campestre* seed design. For manufacturing, a Fused Deposition Modeling (FDM) approach was used. The 3D model was exported in STL format and processed with Prusa Slicer. The internal infill density for the pericarp of the seed was set to 15%, and the print speed was adjusted to 20 mm s^{-1}. A Prusa i3 MKS printer was employed, using a natural and biodegradable filament of polyhydroxyalkanoate (PHA) (ColorFabb). A nozzle with a 0.4 mm diameter was chosen. Compared to the previous biomimetic design,[18] we printed scaled versions of the artificial seed (twice, 2×) to allow for the placement of the fluorescent nanocomposites. The nanocomposites were attached to the pericarp of the printed artificial seeds using ethyl cyanoacrylate as a glue. The morphometric and aerodynamic features of artificial *Acer campestre* were determined according to the methods reported in "Natural *Acer campestre* seed morphometric analysis" and "Determination of the indoor aerodynamic performance of the natural *Acer campestre* seeds."

Luminescence thermometry with fluorescent composites and artificial fliers

The performance of the upconverting nanocomposites was evaluated by monitoring the photoluminescence of the emitters as a function of temperature. The photoluminescence was recorded under identical conditions as for the nanoparticles, except that fluorescent composite discs were placed on a

cooling/heating stage (Linkam Scientific Instruments, THMS 600) where the surface temperature was additionally recorded using an infrared surface thermometer (IR 900 30-S from Voltcraft, Germany). Five photoluminescence spectra were recorded at each temperature.

A proof-of-concept experiment on monitoring the surface temperature of topsoil was performed in a custom-built optical setup. This setup consisted of a NIR laser operating at 980 nm wavelength (RLP-980–300 from Roithner Lasertechnik GmbH, Germany) focusing on the fluorescent nanocomposite attached to the pericarp of the artificial flier, with a collimating lens (74-VIS from Ocean Optics, Germany) achieving a power density of 0.4 W cm^{-2}. The emitted fluorescence was collected using a 400 μm diameter fiber (QP400-2-SRIBX from Ocean Optics, Germany) coupled with a high-resolution spectrometer (HB2000+ from Ocean Optics). The excitation light was removed using a 750 nm short pass dichroic filter (FESHO750 from Thorlabs). The NIR laser was aligned perpendicular to the seeds at approximately 150 cm distance. The fluorescence signal was collected by the fiber at an angle of 60° and a distance of 20 cm and entered the spectrometer where it was recorded with an integration time of 10 s. The artificial fliers were placed flat on the topsoil, and the intensity of the fluorescence was recorded as a function of the temperature of the soil for 12 hours within a laboratory. The temperature of the soil surface was monitored separately using an IR 900 30-S infrared thermometer.

Results and discussion

Upconverting nanoparticles with lanthanide ions (Er^{3+}, Tm^{3+} and Yb^{3+}) doped into tetragonal $BaYF_5$, cubic $NaYF_4$, and cubic CaF_2 hosts were synthesized *via* solvothermal protocols.[20–22] The nanoparticles were coated with oleic acid and dispersed in organic solvents. We ensured that they had high crystallinity and low phonon energies (Fig. S1, SI), prerequisites for reduction of non-radiative processes, and promotion of radiative processes for bright photoluminescence of the emitting lanthanide ions.[1] The diffraction patterns of the hosts indicate minor crystalline impurities (Fig. S1, SI) as is commonly reported for this route.[20,21] The morphology of the particles was determined from transmission electron micrographs (TEMs), revealing rectangular-like shapes with maximal dimensions of 27 ± 5 nm for $BaYF_5$ (Fig. 1A), square-like shapes with dimensions of 17 ± 3 nm for $NaYF_4$ (Fig. 1B), and spherical particles with diameters of 10 ± 2 nm for the CaF_2 host (Fig. 1C).

Upconversion of the nanoparticles was triggered with a 980 nm NIR laser. All nanoparticles displayed the characteristic emission spectra of Er^{3+} and Tm^{3+}.[1] Doping Er^{3+} and Yb^{3+} into tetragonal $BaYF_5$ generated bright green emissions with two typical bands located at 520 nm and 540 nm (Fig. 1D). When these two ions were doped together with Mn^{2+} into a cubic $NaYF_4$ host,[19] a bright red emission became dominant (Fig. 1E). Mn^{2+} ions guide the formation of the cubic phase of the $NaYF_4$ host, in addition to promoting a dominant red emission instead of the usual green emissions of Er^{3+}.[19] Co-doping Tm^{3+} with Yb^{3+} into a cubic CaF_2 host led to the typical blue emissions (Fig. 1F).

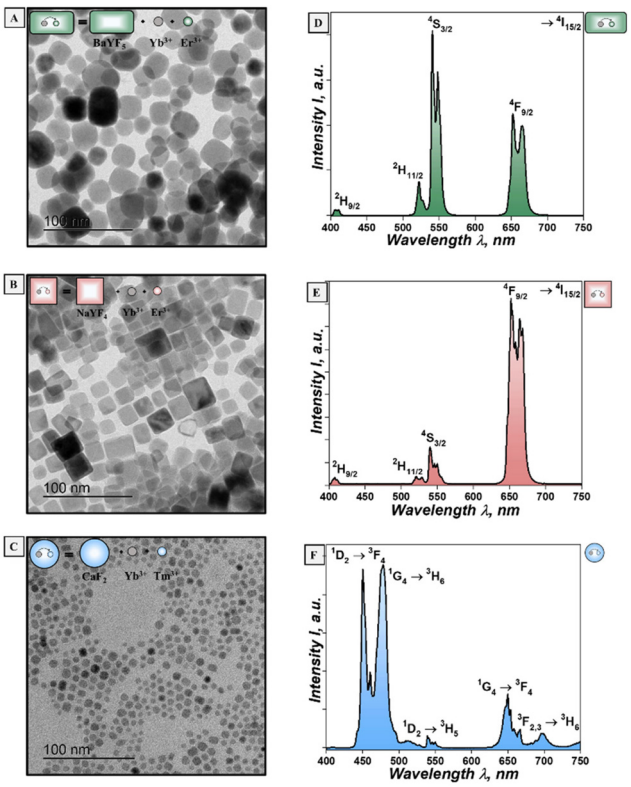

Fig. 1 Transmission electron micrographs (TEMs) and photoluminescence spectra of the upconverting nanoparticles emitting at (A) and (D) green (Er^{3+} and Yb^{3+}:$BaYF_5$, drawn as a green rectangle), (B) and (E) red (Mn^{2+}, Er^{3+}, and Yb^{3+}:$NaYF_4$, drawn as a red square), and (C) and (F) blue (Tm^{3+} and Yb^{3+}:CaF_2, drawn as a blue sphere) wavelengths after excitation at 980 nm wavelength.

In all of these upconverting materials, the Yb^{3+} ion acts as sensitizer by absorbing the 980 nm irradiation that populates the energy levels of the activators (Er^{3+} and Tm^{3+}) *via* energy transfer (ET). Within these energy levels, the electrons populate high-lying levels of the activators ($^4F_{7/2}$ for Er^{3+} and $^1D_2$ for Tm^{3+}), followed by non-radiative relaxation to low-lying levels or radiative relaxation to ground states that causes the characteristic visible emissions in the blue (for Tm^{3+}) or green and red (for Er^{3+}) regions.[1,2]

For the green and red emissions of Er^{3+}, non-radiative decays from $^4F_{7/2}$ can populate $^2H_{11/2}$, $^4S_{3/2}$ and $^4F_{9/2}$ before decaying radiatively to the ground state $^4I_{15/2}$ level, which generates bands at 520 nm, 540 nm and 660 nm, respectively. For the blue emissions of Tm^{3+}, a direct radiative transition from the $^1D_2 \rightarrow {}^3F_4$ level generates the emission at 450 nm, while non-radiative transitions that populate $^1G_4$ enable radiative transition to $^3H_6$ that generates the Stark bands at 460 nm and 475 nm.

Fluorescent nanocomposites were first prepared by combining the nanoparticles with a polymer matrix using a solvent evaporation process.[18,19] Polyhydroxyalkanoate (PHA) was

 This journal is © The Royal Society of Chemistry 2026

selected as the matrix polymer due to its biodegradability, non-toxicity and renewable properties.[16,17] PHA is synthesized through the fermentation of renewable feedstocks like sugars or plant oils.[16,17] The polymer was dissolved in chloroform and the solution mixed with nanoparticle powders (*e.g.* red emitting Mn^{2+}, Er^{3+}, and Yb^{3+} in the $NaYF_4$ host) at different concentrations (1–20 wt%). The dispersions were drop-casted on a Teflon substrate and dried. We created circular composites of 8.0 ± 0.7 mm in diameter with a thicknesses of 200 ± 25 μm and a mass of 3.3 ± 1.0 mg (Fig. 2A).

Nanoparticle filling ratios were optimized to produce a mechanically stable nanocomposite. Excessive filling ratios led to brittle materials and deformation during drying (Fig. S2, SI). We found that 15 wt% nanoparticles resulted in suitable composites (Fig. 2A) with uniform distribution of the particles within the matrix (as confirmed from the SEM and EDX data, Fig. S2, SI) and adequate intensity levels of the upconverting emissions (Fig. 2B and Fig. S2, SI). Higher concentrations likely caused agglomeration and heterogeneous packing.

The photostability of the fluorescent nanocomposites was experimentally evaluated. Lanthanide-doped materials are known to exhibit self-heating upon laser irradiation at 980 nm, which we wanted to exclude.[1–3] We continuously irradiated the fluorescent nanocomposites with a 980 nm laser operating at a power density of 0.4 W cm^{-2}, a value reported to avoid self-heating in upconverting materials.[1–3] The intensities of the emissions at 475 nm, 540 nm and 660 nm for the blue, green and red nanocomposites, respectively, were recorded for 30 h (Fig. S3, SI). After 30 h, the intensities of the green, red and blue single emitters decreased by approximately by 0.8%, 0.3% and 0.5% of their respective original values. These data suggest that the overall composite structure is virtually unaffected by the NIR irradiation at this power density, and 0.4 W cm^{-2} was used in all later measurements.

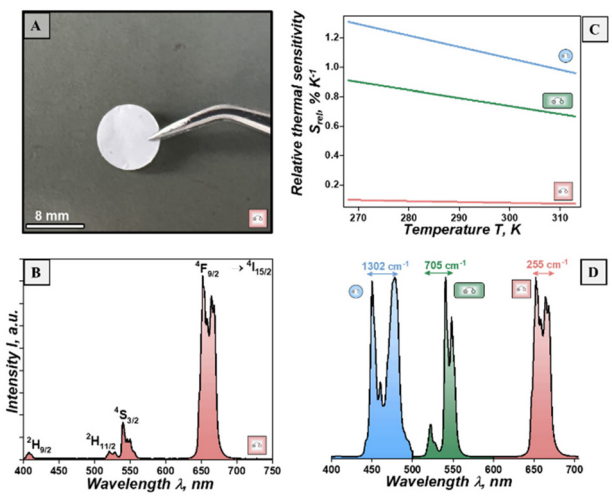

Fig. 2 Fluorescent single-emitter nanocomposites with PHA matrices filled with different types of upconverting nanoparticles. (A) Photograph and (B) upconversion spectra of the fluorescent nanocomposites based on red emitting nanoparticles (Mn^{2+},Er^{3+}, and Yb^{3+}:$NaYF_4$). (C) S_{rel} and (D) illustration of the TCLs and ΔE of the blue (Er^{3+} and Tm^{3+}:CaF_2), green (Er^{3+} and Yb^{3+}:$BaYF_5$) and red (Mn^{2+}, Er^{3+}, and Yb^{3+}:$NaYF_4$) emitters used for the calculation of S_{rel} in (C).

The thermometric performance of the fluorescent composites was determined using S_{rel} that indicates the maximum change of the thermometric parameter (Δ) per degree of temperature change and is calculated as follows:[2,3]

$$S_{rel} = \frac{1}{\Delta}\left|\frac{\partial \Delta}{\partial T}\right| \times 100\% \quad (1)$$

The thermometric parameter is defined as:[2,3]

$$\Delta = \frac{I_1}{I_2} \quad (2)$$

where I_1 and I_2 are the integrated areas of the two emissions used for thermometry. For the TLC-based emitters, Δ depends on ΔE of the emitting levels as:[2,3]

$$\Delta = \frac{I_1}{I_2} = B \cdot \exp\left(-\frac{\Delta E}{k_B T}\right) \quad (3)$$

where k_B is Boltzmann's constant, T is the temperature, and B is an experimental parameter usually determined from the fitting of the experimental data. Section S1 in the SI describes the fitting data and equations to determine S_{rel} in detail.

The thermometric performance of our single emitter nanocomposites was investigated from 268 K to 313 K. For the green emitting composites, S_{rel} depends on the ratio of two TCLs centred at 520 nm and 540 nm (Fig. S4, SI). For the red emitting composites, the Stark sublevels centred at 650–660 nm were used to calculate S_{rel} (Fig. S4, SI). For the blue emitting composites, S_{rel} was based on the Δ calculated from the integral intensities centred at 450 nm and 475 nm (Fig. S4, SI). All three nanocomposites showed relatively low S_{rel} below 1.5% K^{-1} (Fig. 2C). As expected, S_{rel} decreased with increasing operating temperature (eqn (S3), Section I, SI) and was proportional to and limited by the ΔE between the two emission bands used for sensing (eqn (S3), Section I, SI), *i.e.*, 705 cm^{-1}, 255 cm^{-1} and 1302 cm^{-1} for the green, red and blue composites, respectively (Fig. 2D). The small spectral gaps (Stark sublevels on the red composites) or the overlaps (for the blue composites) between the emissions used in sensing limited the discriminability and thus the achievable accuracy.

In the following, we introduce a strategy based on nanocomposites with mixed emitters that avoids spectral overlap and provides more freedom to combine emissions for improved S_{rel}. Upconverting nanoparticles with emissions at the blue, green and red wavelengths were combined to provide easily distinguishable emissions and significantly improve the SNR. This enabled sensitive thermometers with temperature-dependent upconversion spectra that can be tailored to the application. For example, the green and the blue emitters are quenched with temperature, while the red emitters are barely influenced (Section I, SI), because they are not thermally coupled. The small temperature dependence likely is due to multiphonon relaxation pathways that populate the $^4F_{9/2}$ level, which are weakly affected by temperature.[21] Our mixed emitter

nanocomposites exploit these differences to boost the thermometric performance.

We prepared mixed emitter nanocomposites using the same solvent evaporating process as for the single emitters. The fractions of each emitter type were varied at the optimal overall filling ratio of 15 wt% established above and optimized to create mixed nanocomposites with RGB emissions at equivalent intensity levels. Fig. 3 shows a mixed emitter nanocomposite with red (Mn^{2+}, Er^{3+}, and Yb^{3+}:$NaYF_4$) and green (Er^{3+} and Yb^{3+}:$BaYF_5$) emitters as an example. The single emitter red composite with 15 wt% Mn^{2+}, Er^{3+}, and Yb^{3+}:$NaYF_4$ nanoparticles had an emission in the red band (620–680 nm) with an intensity that was nearly 14-fold that the green band (520–570 nm) (labelled as "100% Red", red line, Fig. 3A). We increased the fraction of the green emitters in the mixed emitter composite (Er^{3+} and Yb^{3+}:$BaYF_5$) in three steps to adjust the relative intensities and chose equal fractions of the emitters to obtain the final mixed emitter with aligned band intensities (Fig. 3A). The same adjustments were performed in the blue/green and blue/red mixed emitter nanocomposites (Fig. S5, SI). The low quantum yield of the blue emitting composites required a 9-fold higher concentration in comparison with the red or green emitters in the respective mixtures (Fig. S5, SI).

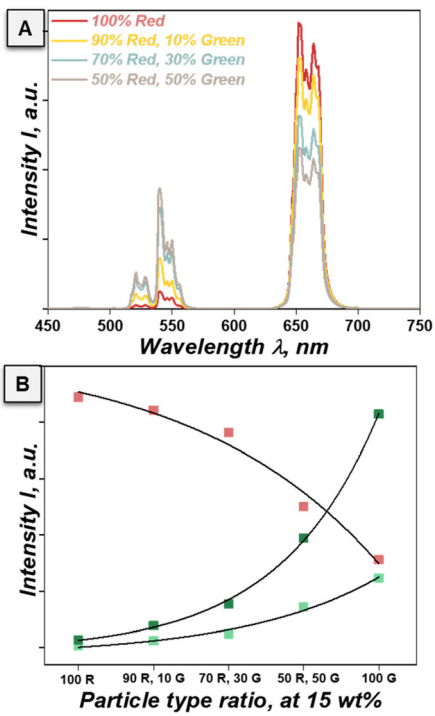

Fig. 3 Mixed emitter nanocomposites for sensitive thermometry with RGB readout. (A) Upconversion spectra and (B) intensities of the 520 nm (light green color), 540 nm (dark green color), and 650 nm (red color) bands of PHA composites containing combinations of red Mn^{2+}-doped Er^{3+} and Yb^{3+}:$NaYF_4$ ("R" for "Red") and green Er^{3+} and Yb^{3+}:$BaYF_5$ ("G" for "Green") nanoparticles as a function of filler fraction at a constant overall 15 wt% filling ratio. All samples were excited with a 980 nm laser operating at 0.4 W cm^{-2}.

Next, we discuss the origin of the overall emission from our mixed emitter nanocomposites. Direct non-radiative energy exchange between different upconverting nanoparticles in the composite is unlikely: Förster or Dexter coupling between the nanoparticles does not occur at particle distances above 5 nm. However, spectral overlaps exist that explain why the overall emission of the mixed emitter nanocomposites is not a linear superposition of the individual particles (Fig. 3B). The green emissions of Er^{3+} can be triggered by the emissions from Tm^{3+} *via* radiative re-absorption. Emissions from Tm^{3+} in Tm^{3+} and Yb^{3+}:CaF_2 in the UV (340–380 nm), blue (450–500 nm), red (650–670 nm), and NIR regions (at 800 nm) (Fig. S6, SI) may overlap with the Er^{3+} absorption bands in the UV (300–400 nm), blue (400–500 nm), and NIR regions (800 nm, 980 nm and 1520 nm).[26–29] We would thus expect that some emissions from Tm^{3+} is absorbed by Er^{3+} to emit green and/or red. Finally, the filling ratio is large enough that relevant wavelength-dependent scattering may occur despite the dispersed state of the nanoparticles in the polymer matrix, introducing additional non-linearity.

The thermometric performance of the mixed composites was evaluated between 268 K and 313 K. Fig. S7 (SI) shows the integrated blue (450–500 nm), green (520–570 nm) and red emissions (from 620 nm to 680 nm) as a function of temperature. The intensity responses to temperature were non-linear in general. The intensity of the green emissions from "50% Red and 50% Green" mixed emitters (hereafter green/red) increased by nearly 5% and then continuously decreased (Fig. 4A). A similar trend was also detected for the green/blue mixed emitters (Fig. S7, SI). For the mixture of blue and red emitters, a more linear decrease was detected (Fig. S7, SI). These non-linear trends are expected due to the spectral overlaps of the activators, as explained above.

We defined thermometric parameters Δ_i as the ratios between the integral intensities of the blue *vs.* green (Δ_1), blue *vs.* red (Δ_2) and green *vs.* red (Δ_3) bands (Section S2 and Table S2, SI). These ratios are based on energy levels that arise from different emitting ions embedded into different hosts and have ΔE above 2000 cm^{-1},[30] *i.e.*, they are non-thermally coupled levels (NTCLs). Their temperature dependencies are commonly described using empirical polynomials.[30] All experimental Δ_i values for the NTCLs were thus fitted to the following equation:

$$\Delta_i = \frac{a_i + b_i T}{1 + c_i T + d_i T^2} \quad (4)$$

where a_i, b_i, c_i, and d_i are empirical constants. The thermometric performance of the mixed composites was evaluated by calculating the figures of merit S_{rel}, the temperature resolution δT and the repeatability R using eqn (S6), (S7), (S8), respectively (Section S2, SI).[2,3]

The intensity ratios of all three mixed nanocomposites decreased with increasing temperature (Fig. 4B). The decrease of the intensity ratio was the largest for the blue/green composites (Δ_1, symbols in purple in Fig. 4B). The composite formed from Δ_1 achieved a high value of S_{rel} (eqn (S6), SI) in the range of 33.9 ± 1.3% K^{-1} at 268 K (Fig. 4C). The green/red (Δ_3) com-

This journal is © The Royal Society of Chemistry 2026

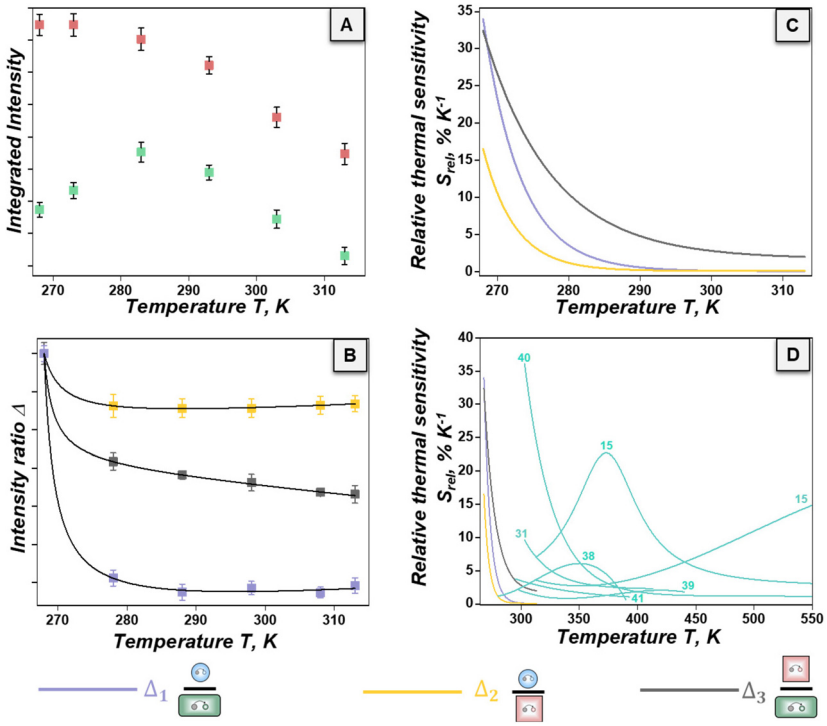

Fig. 4 Thermometric performance of mixed emitter nanocomposites: (A) integrated intensities of the green (520–570 nm, green) and red (620–680 nm, red) emissions from the green/red mixed composites as an example (*cf.* the SI for all other wavelengths), (B) intensity ratios Δ_i (symbols are the experimental data and the solid line is the polynomial fit with eqn (4)) and (C) $S_{rel,i}$ as a function of temperature. (D) Comparison of the state-of-the-art S_{rel} of thermometers based on NTCLs (blue lines) with our mixed emitters. The numbers indicate the references containing the respective S_{rel} values.

posites (grey line) had S_{rel} values of around 32.5 ± 1.6% K^{-1} at the same temperature. The composite formed from the blue and red (Δ_2) emitters (yellow line) showed the lowest value of S_{rel} of approximately 16.5 ± 1.7% K^{-1} (Fig. 4C).

The temperature resolution, δT, indicates the lowest temperature change that a thermometer can resolve.[2,3] δT is inversely proportional to S_{rel} and proportional to the relative uncertainty of the intensity ratio (eqn (S7), SI). Its values for the Δ_1, Δ_2 and Δ_3 nanocomposites were 0.014 K, 0.030 K, and 0.015 K at 268 K, respectively. The blue/green composites provided the smallest resolution, mainly due to their high S_{rel} (eqn (S7), SI). Thus, our mixed emitter composites reach temperature resolutions that are approximately 10–20-fold higher compared to state-of-the-art-based thermometers.[15,31]

The repeatability R indicates the ability of a thermometer to provide the same temperature measurement at different times under identical conditions.[2,3] It is commonly estimated by comparing readings during repeated heating/cooling cycles and calculating the values of Δ or S_{rel}. Eqn (S8) (SI) indicated an R value in the range between 96 and 98% for 5 cycles (Fig. S8, SI and Table S1, SI with a summary on the fitting parameters, S_{rel}, δT and R for these mixed composites). State-of-the-art thermometers achieve similar R values,[15,31] although not all reports contain quantitative data.

In the following, we compare the performances of different mixed emitter nanocomposites and the state-of-the-art using S_{rel} because it is a widely applied figure of merit independent of operating wavelengths, acquisition setup or nature of the materials employed as thermometers.[2,3]

The maximal S_{rel} values of our mixed emitters were approximately 40 times those of green Er^{3+} and Yb^{3+} in $NaYF_4$,[32] or in $NaY(WO_4)_2$ emitters,[33] in exiting TCL thermometers (Fig. S9, SI). They were 70 times higher than those of blue emitters with Tm^{3+} and Yb^{3+} in $NaLuF_4$,[34] or in Y_2O_3,[35] and 6 times than those of red (Tm^{3+} in $NaYb(MoO_4)_2$[36]) and NIR (Nd^{3+} in LaF_3) emitters.[37]

The relative thermal sensitivities of state-of-the-art NTCL-based thermometers with blue Tm^{3+} in $NaGdF_4$@$NaYF_4$ and green emitting Er^{3+} in $NaYF_4$ in a poly(methyl methacrylate) (PMMA) matrix,[38] or when co-doped in molybdate hosts,[39] have S_{rel} of up to 5.88% K^{-1} at 339 K (turquoise lines, Fig. 4D), approximately 5 to 6 times lower than our mixed emitters. A high S_{rel} of 36.2% K^{-1} at 303 K was recorded when the blue emission (474 nm) and deep red emission (696 nm) of Tm^{3+} were combined in a $NaLaTi_2O_6$ host[40] (turquoise lines, Fig. 4D).

NTCLs based on core@shell nanoparticles emitting at different wavelength regions with emissions in the Vis and NIR regions (turquoise line, Fig. 4D) have been introduced. An active core@inert shell Yb^{3+}:$NaErF_4$@$NaYF_4$ nanostructure achieved an S_{rel} of 3.76% K^{-1} at 295 K using the NTCLs of Er^{3+} at 540 nm and 1527 nm.[41] An even more complex single structure (an active core@inert shell@active shell Er^{3+} and Yb^{3+}:

$NaYF_4$@$NaYF_4$@$NaYF_4$:Yb^{3+} and Nd^{3+}) was used as a thermal probe based on the quench "on" of the red emission of Er^{3+} (654 nm) and quench "off" of the NIR emission of Nd^{3+} (803 nm).[31] These opposite trends led to an S_{rel} of 9.6% K^{-1} at 303 K.[31]

Recently, two different materials with quench "off" and "on" properties were embedded within a hydrogel.[15] Quench "off" was assigned to the emission of Er^{3+} (540 nm) within the Er^{3+} and Yb^{3+}:$NaYF_4$@$NaYF_4$ nanostructures. Quench "on" was due to the emission of either Nd^{3+} (799 nm) or Tm^{3+} (796 nm) doped within the 3 μm $Yb_2W_3O_{12}$ microparticles. The ratio among Er^{3+} and Nd^{3+} achieved a maximum S_{rel} of 15.3% K^{-1} at 553 K. A boost in S_{rel} was achieved (23.84% K^{-1} at 380 K) for the ratio among Er^{3+} (540 nm) and Tm^{3+} (796 nm) (turquoise lines, Fig. 4D).[15]

Despite these high values of S_{rel} in the state-of-the-art thermometers, our mixed emitter thermometers based on Δ_1 (purple line, Fig. 4D) and Δ_3 (gray line, Fig. 4D) are more sensitive (turquoise lines, Fig. 4D). Furthermore, our thermometers do not require complex core@shell particle architectures that are harder to optimize in terms of dopants (either sensitizers or activators). The NTLC thermometers described above require concurrent Vis/NIR optics to be properly readout. Our mixed emitter nanocomposites are fully operative within the Vis range of the spectrum. In addition, detectors such as silicon photodiodes and CCD or CMOS cameras for Vis light are cheaper compared to InGaAs detectors for NIR light.[42]

A current limitation of our mixed emitter concept is the temperature range with high S_{rel} (268–290 K): the sensitivity drops to 0.05%–1% K^{-1} above 300 K (Fig. 4C and D). This temperature range can be extended by combining more than two emitters or designing hosts with a negative thermal expansion coefficient to trigger Vis emissions with quench "on" properties. In this contribution, we limited ourselves to mixed emitter composites for maximal sensitivity in the environmental temperature range because we were primarily interested in their application for environmental sensing.

We evaluated the application of the mixed emitters as sensitive elements in environmental probes. Current technologies for environmental sensing rely on complex materials that generate e-waste.[43] Recently, self-deployable and biocompatible artificial seeds inspired by plants, are growing as alternative probes.[18,19,44] These seeds mimic the properties of the natural plants. They react optically to environmental parameters and are read using drones equipped with fluorescence light detection and ranging (fLIDAR) technology placed on a distance. The artificial seeds can remain in the field where they degrade and cause no harm.[18,19,44]

It has been shown previously that passive fliers can be designed by creating artificial seeds inspired by natural *Acer campestre* (or samara). These seeds fly with the wind and are able to cover large distances and areas.[45] Artificial and fluorescent *Acer campestre* seeds (or fliers) have previously been produced *via* 3D printing technologies to monitor the temperature of topsoil.[18] The whole body of the artificial seed was constructed on commercial lanthanide-doped particles (approximately 3 μm in size).[18] The temperature of the topsoil was deduced based on the TCLs of Er^{3+} ions at 520 nm and 540 nm.[18] The single emitter composites used in these seeds had a limited S_{rel}; however, which limited the distance between the probe and the optical reader. In practice, it made it necessary to fly a drone closely to the seed to record photoluminescence with sufficient SNRs for the analysis of the two green bands, which is difficult. Here, we address these limitations by 3D printing artificial *Acer campestre* seeds and attach them into the mixed emitter nanocomposites with a high SNR and a high S_{rel}.

Starting from the images of the natural *Acer campestre* seeds (Fig. 5), we drew a vectorized contour, followed by creating a vector file of the contours (Fig. 5). Then, a 3D CAD model was developed for the design of the artificial samara seeds. The CAD model was converted into a STL format and sliced. A model was extruded and scaled up to 2× of the original dimensions of the natural seeds with the goal of allowing for a large area for coupling with the fluorescent sensors (Fig. 5). The artificial seeds were printed using PHA as a polymer. The fluorescent nanocomposite was coupled at both sides of the printed *Acer campestre* seed using ethyl cyanoacrylate as a glue. The morphometric and aerodynamic characteristics of the unit (the seed and the fluorescent nanocomposite) were analyzed.

Acer campestre seeds are composed of a pericarp (marked with "1" in Fig. 6A) and a wing (marked with "2" in Fig. 6A). The morphological and physical characteristics of the natural

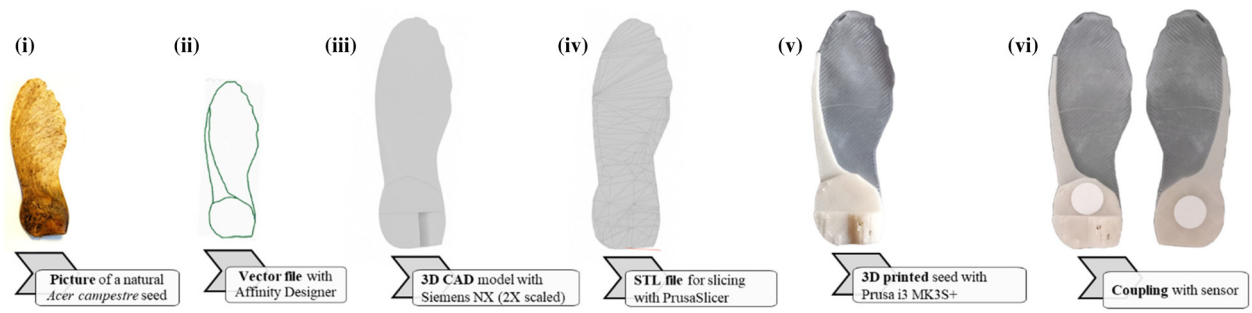

Fig. 5 Development of the artificial seeds starting from the natural *Acer campestre* species. The flowchart consists of (i) the picture of natural *Acer campestre*, (ii) vector file extract from the contours, (iii) creation of 2× scaled CAD files, (iv) creation of 2× scaled STL files, (v) 3D printing of 2× scaled artificial *Acer campestre* using PHA, and (vi) integration of the fluorescent nanocomposite using ethyl cyanoacrylate as a glue.

This journal is © The Royal Society of Chemistry 2026

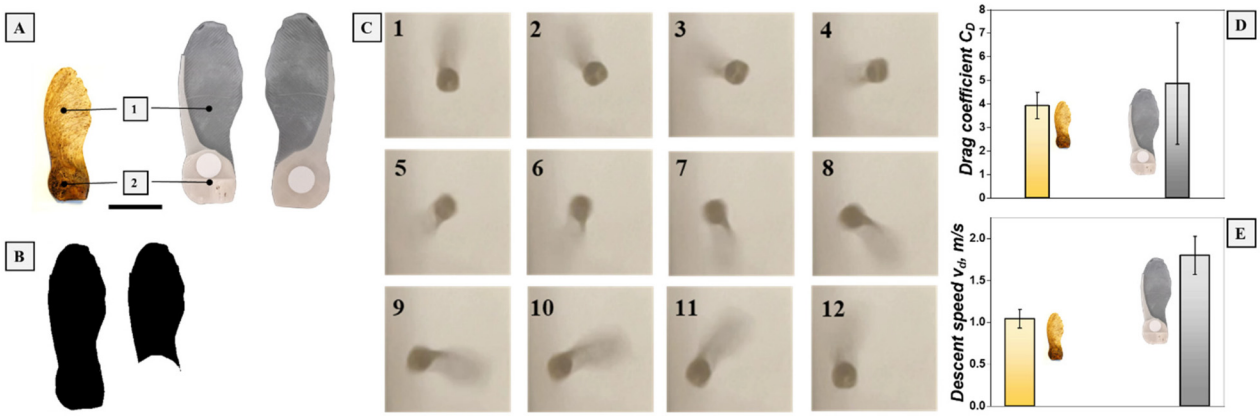

Fig. 6 Morphometric and aerodynamic characterization of natural and artificial *Acer campestre* seeds. (A) Natural *Acer campestre* seed composed of a capsule and a wing (under "**1**") and a wing (under "**2**"). (B) Image binarization of the complete seed and the wing for estimation of the wing surface (*S*) and the wing loading (*W*/*S*). (C) Twelve frames of the descent of the sensing seed for measuring the rotational velocity. Comparison of (D) the drag coefficient (C_D) and (E) the descent speed (v_d) of the natural and artificial seeds.

seeds were determined to guide the process of printing the artificial seeds (Fig. S10, SI).[18] In short, the average mass was 56 ± 11 mg (from 10 seeds). The average value of the wing surface (*S*), estimated from wing image binarization, was 173 ± 21 mm^2. The wing loading (*W*/*S*), with a weight (*W*) of 0.549 ± 0.1 × 10^{-3} N was 3.17 ± 1.01 N m^{-2}. In terms of their aerodynamic characteristics, the lab descent speed (v_d), rotational velocity (Ω), wing tip speed (v_t) and drag coefficient (C_D) were 1.04 ± 0.11 m s^{-1}, 160.5 ± 23.3 rad s^{-1}, 3.94 ± 0.57 m s^{-1}, and 4.87 ± 2.58, respectively, in accordance with our previous results.[24,25]

The total mass (*m*) of the flier with the artificial seed and the sensing unit was 703.1 ± 9.3 mg and the mean *S* was 709 ± 31 mm^2 (Fig. 6B). The *W*/*S* of the printed flier was 9.72 ± 0.55 N m^{-2}, while the Ω (Fig. 6C), v_t and C_D values were 144.1 ± 15.3 rad s^{-1} (Movie S1, SI), 7.00 ± 0.79 m s^{-1}, and 4.99 ± 1.53, respectively. Both v_t and C_D values resulted statistically equal for natural and artificial seeds (Fig. 6D), as the v_d of the artificial fliers was 1.80 ± 0.23 m s^{-1}, approximately 80% more than the natural level (Fig. 6E), consistent with a more than 10-fold increase in mass. All results (Table S2, SI) imply the potential to print fluorescent artificial seeds that mimic the properties of the natural seeds by preserving the same design, regardless of the weight, dimensions and addition of the fluorescent nanocomposites. After integrating the fluorescent sensors into the artificial seeds, we conducted a proof-of-concept experiment. A distributed environmental sensing scenario was emulated by monitoring the surface temperature of topsoil with a printed fluorescent artificial seed. A freshly collected soil sample was placed on a flat surface (Fig. 7A). The seed with a fluorescent composite containing a green/red mixture was placed on top. These emitters have a higher quantum yields compared to the blue nanoparticles. The seed was irradiated with a 980 nm laser (power density 0.4 W cm^{-2}) using a custom-built optical setup to guide the beam perpendicular to the position of the fluorescent composite on the seed. The dis-

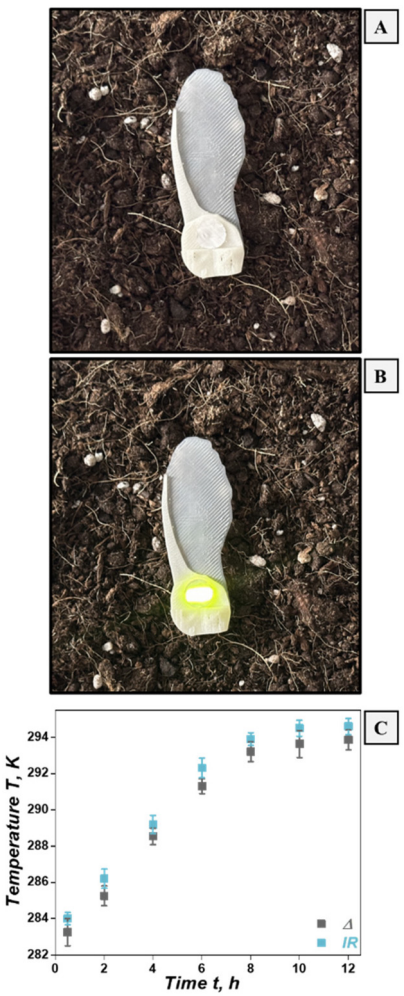

Fig. 7 Monitoring the surface temperature of topsoil with the fluorescent artificial seeds: (A) on topsoil, (B) irradiated with a 980 nm laser, and (C) temperature of the topsoil determined from the fluorescent seeds ("*Δ*" in gray) and from a reference external infrared thermometer ("IR" in blue).

tance between the laser and the fluorescent seed was approximately 150 cm. Its lime-coloured emission (Fig. 7B) was recorded using a high-resolution Ocean Optics spectrometer (HB2000+) coupled with a flexible 400 μm diameter fiber. The soil was collected at low temperature in the morning (approximately 280 K) that slowly increased to room temperature within the controlled environment of a laboratory (295 K). The temperature of the topsoil was monitored using a reference external infrared thermometer ("IR", Fig. 7C).

The fluorescent seed was continuously irradiated with the NIR laser for a total of 12 hours, and the thermometric parameter Δ was calculated using the ratio among the green and red bands as in Δ_3 and averaged in 10 min intervals. Based on the calibration curve of Δ_3, the topsoil temperatures were calculated ("Δ", Fig. 7C). The mean differences between optical thermometry and the IR camera were 0.5 K to 0.8 K after 5 repetitions of the experiment (Fig. 7C). Part of this is due to the low thermal conductivity of the PHA polymer (0.10–0.25 W m^{-1} K^{-1}),[46] which leads to a slow heat transfer. This result indicates that fluorescent artificial fliers are a suitable platform for monitoring the surface temperature of topsoil within the narrow environmental range and can be applied for outdoor sensing with drones equipped with fLIDAR (Movie S2, SI).

Conclusions

In summary, we demonstrated that bright upconverting nanocomposites can be used to create plant-inspired artificial fliers that act as sensitive thermometers to monitor the surface temperature of topsoil. The nanocomposites were based on red, green and blue upconverting emitters and a biodegradable PHA polymer. By mixing the emitters, we created fluorescent nanocomposites with clearly distinguishable emission signals, high SNRs and S_{rel} up to 34% K^{-1}, overcoming current limitations of the state-of-the-art thermometers. Integrating these thermometers into the artificial fliers confirmed that they are suitable for environmental monitoring.

The artificial seeds created here have mixed emitter nanocomposites attached on the pericarp. It is also possible to make artificial fliers entirely out of the fluorescent nanoparticles, for example, by direct ink writing and density reduction with a leaching process,[44] or by using lightweight aerogels that are formed *via* freeze-drying.[47]

The mixed emitter nanocomposites that we introduced here are designed for environmental temperatures and limited in their operational range. The concept is more versatile: combinations with more than two emitters and with particles that have thermal quench "on" and quench "off" properties are possible to extend and tune their temperature range.

Author contributions

Albenc Nexha and Stefano Mariani wrote the original draft of the manuscript. Albenc Nexha and Anja Colbus performed the experiments on the upconverting nanoparticles, preparation of the composites and luminescence thermometry. Stefano Mariani and Kliton Cikalleshi worked on the production and characterization of the artificial seeds. All authors took part in the conceptualization, reviewing, and editing of the manuscript. Barbara Mazzolai and Tobias Kraus led the supervision and funding acquisition.

Conflicts of interest

There are no conflicts to declare.

Data availability

The data that support the findings of this study will be made available upon request from the corresponding authors.

Supplementary information (SI) is available. See DOI: https://doi.org/10.1039/d6nr00489j.

Acknowledgements

This project has received funding from the European Union's Horizon 2020 Research and Innovation Programme under grant agreement no. 101017940 (I-Seed).

References

1 G. Chen, H. Qiu, P. N. Prasad and X. Chen, *Chem. Rev.*, 2014, **114**, 5161–5214.
2 A. Nexha, J. J. Carvajal, M. C. Pujol, F. Díaz and M. Aguiló, *Nanoscale*, 2021, **13**, 7913–7987.
3 A. Nexha, M. C. Pujol Baiges and J. J. Carvajal Martí, in *Luminescent Thermometry: Applications and Uses*, ed. J. J. Carvajal Martí and M. C. Pujol Baiges, Springer International Publishing, Cham, 2023, pp. 221–268. DOI: 10.1007/978-3-031-28516-5_6.
4 H. Suo, X. Zhao, Z. Zhang, Y. Wang, J. Sun, M. Jin and C. Guo, *Laser Photonics Rev.*, 2021, **15**, 2000319.
5 M. L. Debasu, D. Ananias, I. Pastoriza-Santos, L. M. Liz-Marzán, J. Rocha and L. D. Carlos, *Adv. Mater.*, 2013, **25**, 4868–4874.
6 O. A. Savchuk, J. J. Carvajal, M. C. Pujol, E. W. Barrera, J. Massons, M. Aguilo and F. Diaz, *J. Phys. Chem. C*, 2015, **119**, 18546–18558.
7 M. Suta, Ž Antić, V. Đorđević, S. Kuzman, M. D. Dramićanin and A. Meijerink, *Nanomaterials*, 2020, **10**, 543.
8 C. D. S. Brites, P. P. Lima, N. J. O. Silva, A. Millán, V. S. Amaral, F. Palacio and L. D. Carlos, *Adv. Mater.*, 2010, **22**, 4499–4504.
9 Y. H. Han, C. B. Tian, Q. H. Li and S. W. Du, *J. Mater. Chem. C*, 2014, **2**, 8065–8070.
10 S. Zheng, W. Chen, D. Tan, J. Zhou, Q. Guo, W. Jiang, C. Xu, X. Liu and J. Qiu, *Nanoscale*, 2014, **6**, 5675–5679.

 This journal is © The Royal Society of Chemistry 2026

11 A. Nexha, J. J. Carvajal, M. C. Pujol, F. Díaz and M. Aguiló, *J. Mater. Chem. C*, 2021, **9**, 2024–2036.
12 O. A. Savchuk, J. J. Carvajal, C. D. S. Brites, L. D. Carlos, M. Aguilo and F. Diaz, *Nanoscale*, 2018, **10**, 6602–6610.
13 T. Y. Sun, D. Q. Zhang, X. F. Yu, Y. Xiang, M. Luo, J. H. Wang, G. L. Tan, Q. Q. Wang and P. K. Chu, *Nanoscale*, 2013, **5**, 1629–1637.
14 E. N. Cerón, D. H. Ortgies, B. del Rosal, F. Ren, A. Benayas, F. Vetrone, D. Ma, F. Sanz-Rodríguez, J. G. Solé, D. Jaque and E. M. Rodríguez, *Adv. Mater.*, 2015, **27**, 4781–4787.
15 Y. Wang, L. Lei, R. Ye, G. Jia, Y. Hua, D. Deng and S. Xu, *ACS Appl. Mater. Interfaces*, 2021, **13**, 23951–23959.
16 H. Park, H. He, X. Yan, X. Liu, N. S. Scrutton and G.-Q. Chen, *Biotechnol. Adv.*, 2024, **71**, 108320.
17 M. Fernandes, A. Salvador, M. M. Alves and A. A. Vicente, *Polym. Degrad. Stab.*, 2020, **182**, 109408.
18 K. Cikalleshi, A. Nexha, T. Kister, M. Ronzan, A. Mondini, S. Mariani, T. Kraus and B. Mazzolai, *Sci. Adv.*, 2023, **9**, eadi8492.
19 A. Nexha, S. Mariani, K. Cikalleshi, T. Kister, B. Mazzolai and T. Kraus, *Nanoscale*, 2025, **17**, 18143–18152.
20 M. Mo, Y. Liwen, R. Guozhong, X. Changfu, L. Jianguo and Y. Qibin, *J. Lumin.*, 2011, **131**, 1482–1486.
21 G. Tian, Z. Gu, L. Zhou, W. Yin, X. Liu, L. Yan, S. Jin, W. Ren, G. Xing, S. Li and Y. Zhao, *Adv. Mater.*, 2012, **24**, 1226–1231.
22 G. Wang, Q. Peng and Y. Li, *J. Am. Chem. Soc.*, 2009, **131**, 14200–14201.
23 C. A. Schneider, W. S. Rasband and K. W. Eliceiri, *Nat. Methods*, 2012, **9**, 671–675.
24 S. J. Lee, E. J. Lee and M. H. Sohn, *Exp. Fluids*, 2014, **55**, 1718.
25 G. K. Nave, N. Hall, K. Somers, B. Davis, H. Gruszewski, C. Powers, M. Collver, D. G. Schmale and S. D. Ross, *Biomimetics*, 2021, **6**, 23.
26 B. V. N. Kumar and R. E. Kroon, *Opt. Mater.*, 2025, **167**, 117274.
27 A. S. Nizamutdinov, A. A. Shavelev, A. V. Astrakhantseva, K. N. Boldyrev, A. G. Nikolaev, E. B. Dunina, A. A. Kornienko, A. A. Pynenkov, A. A. Lyapin, S. V. Kuznetsov and V. V. Semashko, *Opt. Mater.*, 2024, **147**, 114585.
28 H. Xia, J. Feng, Y. Wang, J. Li, Z. Jia and C. Tu, *Sci. Rep.*, 2015, **5**, 13988.
29 R. T. Wegh, A. Meijerink, R. J. Lamminmäki and H. Jorma, *J. Lumin.*, 2000, **87–89**, 1002–1004.
30 G. Xiang, Y. Yi, Z. Yang, Y. Wang, L. Yao, S. Jiang, X. Zhou, L. Li, X. Wang and J. Zhang, *Inorg. Chem. Front.*, 2024, **11**, 1522–1530.
31 C. Mi, J. Zhou, F. Wang, G. Lin and D. Jin, *Chem. Mater.*, 2019, **31**, 9480–9487.
32 L. Li, F. Qin, Y. Zhou, Y. Zheng, H. Zhao and Z. Zhang, *ACS Appl. Nano Mater.*, 2018, **1**, 1912–1920.
33 M. Lin, L. Xie, Z. Wang, B. S. Richards, G. Gao and J. Zhong, *J. Mater. Chem. C*, 2019, **7**, 2971–2977.
34 H. Lu, H. Hao, G. Shi, Y. Gao, R. Wang, Y. Song, Y. Wang and X. Zhang, *RSC Adv.*, 2016, **6**, 55307–55311.
35 G. Chen, R. Lei, F. Huang, H. Wang, S. Zhao and S. Xu, *Luminescence*, 2018, **33**, 1262–1267.
36 M. Jia, Z. Sun, H. Xu, X. Jin, Z. Lv, T. Sheng and Z. Fu, *J. Mater. Chem. C*, 2020, **8**, 15603–15608.
37 E. Carrasco, B. del Rosal, F. Sanz-Rodríguez, Á. J. de la Fuente, P. H. Gonzalez, U. Rocha, K. U. Kumar, C. Jacinto, J. G. Solé and D. Jaque, *Adv. Funct. Mater.*, 2015, **25**, 615–626.
38 E. D. Martínez, C. D. S. Brites, L. D. Carlos, A. F. García-Flores, R. R. Urbano and C. Rettori, *Adv. Funct. Mater.*, 2019, **29**, 1807758.
39 Z. Zhang, D. Zhu, Z. Huang, Z. Zhu, J. Liu and K. Li, *Mater. Today Chem.*, 2025, **48**, 102971.
40 K. Li, Z. Zhang, D. Zhu and C. Yue, *Inorg. Chem. Front.*, 2024, **11**, 7464–7474.
41 Y. Wang, L. Lei, E. Liu, Y. Cheng and S. Xu, *Chem. Commun.*, 2021, **57**, 9092–9095.
42 B. Zhu and H. Jonathan, *Sensors*, 2024, **24**, 3539.
43 R. Ouni and K. Saleem, *Sustainability*, 2022, **14**, 8356.
44 S. Mariani, K. Cikalleshi, M. Ronzan, C. Filippeschi, G. A. Naselli and B. Mazzolai, *Small*, 2025, **21**, 2403582.
45 K. Yasuda and A. Azuma, *J. Theor. Biol.*, 1997, **185**, 313–320.
46 X. Liang, D. K. Cha and Q. Xie, *Resour. Conserv. Recycl. Adv.*, 2024, **21**, 200206.
47 G. Gallo, R. Tu, C. Filippeschi, S. Mariani and B. Mazzolai, *Adv. Sci.*, 2026, **13**, e08949.

This journal is © The Royal Society of Chemistry 2026